JGR Solid Earth

RESEARCH ARTICLE
10.1029/2019JB018544

Normalized Radiated Seismic Energy From Laboratory Fracture Experiments on Opalinus Clayshale and Barre Granite

Bing Q. Li[1,2] **and Herbert H. Einstein**[2]

[1]Division of Geological and Planetary Sciences, California Institute of Technology, Pasadena, CA, USA, [2]Department of Civil and Environmental Engineering, Massachusetts Institute of Technology, Cambridge, MA, USA

Key Points:
- We estimate radiated seismic energy normalized by external work done for various loading mechanisms in Barre granite and Opalinus clayshale
- The normalized radiated seismic energy emitted from Opalinus clayshale is 3–22% of that in Barre granite across multiple loading mechanisms
- We find beam bending to be highest in normalized radiated seismic energy and the low injection rate hydraulic fracturing the lowest

Supporting Information:
- Supporting Information S1

Correspondence to:
B. Q. Li,
bingqli@caltech.edu

Citation:
Li, B. Q., & Einstein, H. H. (2020). Normalized radiated seismic energy from laboratory fracture experiments on Opalinus clayshale and Barre granite. *Journal of Geophysical Research: Solid Earth*, *125*, e2019JB018544. https://doi.org/10.1029/2019JB018544

Received 15 AUG 2019
Accepted 20 FEB 2020
Accepted article online 21 FEB 2020

Abstract We evaluate the radiated seismic energy normalized by external work for hydraulic fracturing, beam bending, and uniaxial compression experiments conducted on Opalinus clayshale and Barre granite specimens. Results suggest that normalized radiated seismic energy is highest for the beam bending, followed by uniaxial compression, and, finally, that the hydraulic fracturing experiments radiate the least seismic energy when normalized by external work. We also find that the normalized radiated energy during tests on Opalinus clayshale is 3% to 22% of that in Barre granite across multiple loading mechanisms.

1. Introduction

Seismic monitoring and its related applications are major sources of information on the growth of faults and fractures at depth. At the kilometer scale, geophone recordings provide us with insights into the mechanisms behind large-scale earthquakes. At the decameter and meter scale, the energy industries employ microseismic monitoring to detect the evolution of hydraulic fractures that are used to enhance the permeability of tight shale and geothermal reservoirs. At the submeter scales, acoustic emission monitoring is used to detect the growth of fractures in concrete structures and as a laboratory analog to better understand larger-scale seismicity.

At each of these scales, one of the important questions to scientific inquiry and engineering design revolves around the relationship between seismicity and how this seismicity relates to the physical phenomena driving the seismicity, for example, the proportion of seismic to aseismic slip along faults and fractures at depth. For example, the hydrocarbon industry is interested in how well microseismicity reflects the extent of permeability enhancement through hydraulic fracturing (HF) (Teran & Thornton, 2019), while geothermal heat extraction (Grigoli et al., 2018), carbon sequestration (Mazzoldi et al., 2012), and wastewater injection (Ellsworth, 2013) communities require a better understanding of how fluid injection relates to induced earthquakes with magnitudes up to $M_w = 5.8$. At the tectonic scale, there is similarly an interest in the distribution of seismic and aseismic slip (Thomas et al., 2014) on faults at depth.

Recent laboratory studies have shown that there is significant similarity between the lab and field scales on key seismic parameters; for example, Yoshimitsu et al. (2014) found that the physical processes at these scales were highly similar in that the seismic moment is inversely proportional to the cube of the corner frequency. Among hydraulic fracture experiments, Goodfellow et al. (2015) suggest that the seismic energy radiated as a proportion of the injection energy during HF scales is consistent between the laboratory and the field scales at around 1×10^{-7}% to 1×10^{-5}% and that the seismic moment of the recorded microseisms are log-proportional to the injected fluid volume across scales. The radiated seismic energy approach has since been employed by researchers such as Jestin et al. (2019) to study the seismicity of tensile fractures propagating through material interfaces, where they found that seismic efficiency increases with the square root of crack velocity. This study presents results from the application of these methods to different failure mechanisms and rock materials, in order to better understand the seismicity of these processes.

In order to compile and compare results from various experiments on different rocks and loading conditions, we calculate the energy budget in each experiment by considering the fraction of the work done by the loading machine or fluid injection ($\tilde{E}$) that is released as radiated seismic energy (E_R). The main goals

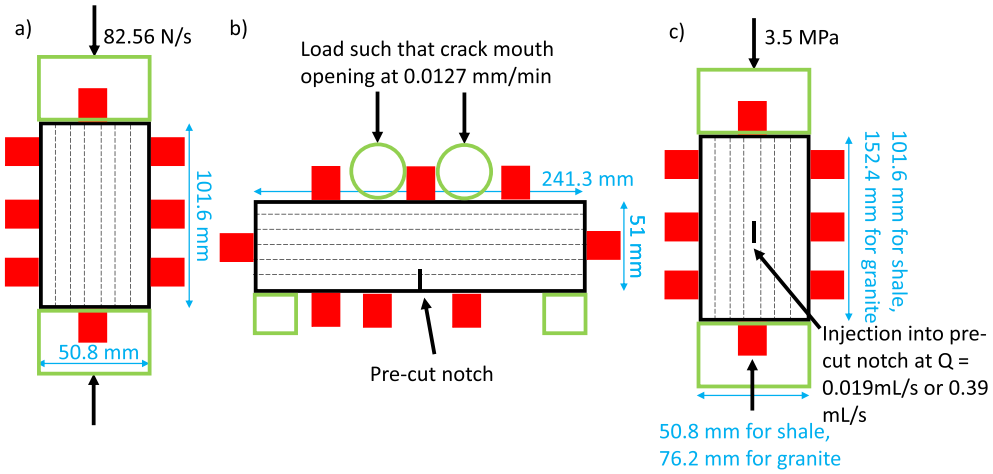

Figure 1. Schematic of test setup for (a) uniaxial compression tests, (b) four-point beam bending tests, and (c) hydraulic fracture tests. Dotted lines indicate bedding plane direction for Opalinus clayshale specimens. Red rectangles indicate AE sensor locations, and green shapes indicate loading platens.

are twofold: First, we would like to determine whether the difference in seismic energy between Opalinus clayshale and Barre granite is consistent across loading conditions. These rocks are chosen as they are analogous to tight shale and the rocks in geothermal reservoirs, respectively. Second, we observe that HF tends to produce fewer AE than beam bending or uniaxial compression experiments and investigate whether this is proportionally lower as a result of the smaller work done by fluid injection compared to loading experiments. Specifically, we consider four types of experiments in our study: HF tests at constant in situ stress under two different injection rates, beam bending tests that apply indirect tensile stress under dry conditions and uniaxial compression tests where the material fails through crushing and shear mechanisms under dry conditions. While many previous studies concentrate on individual materials and loading mechanisms, the framework presented in our study facilitates direct comparison between studies originally designed with differing intents. As a direct example, the vast literature on intact fracture of crystalline rocks may now be compared in the same context to the vast literature on HF of sedimentary rocks.

2. Methods

2.1. Materials

In terms of the materials, the Barre granite consists (Goldsmith et al., 1976) primarily of quartz (31.9%), potash feldspar (17.8%), plagioclase (36.5%), biotite (8%), muscovite(3%), and granophyre (2.8%). The grain sizes generally fall within 2–4 mm (Murthy, 1957), and porosity was estimated at 0.41%. The Opalinus clayshale is obtained from the Mont Terri Underground Research Laboratory in the Jura mountains in Switzerland, at a depth of 200 m below the present surface. The mineralogy was analyzed by James Hutton Limited using X-ray diffraction, who reported 47% quartz, 13.5% calcite, 9.7% kaolinite, and 16.2% illite and illite/smectite. Porosity was estimated at 18.3%.

2.2. Experimental Setup

2.2.1. Physical Setup

In this study, we consider a number of experiments, many of which have been documented in previous publications: uniaxial compression tests on Barre granite and Opalinus clayshale as outlined in this section, beam bending tests on Barre granite (Li & Einstein, 2017) and Opalinus clayshale (Li, 2019), and HF tests on Barre granite and Opalinus clayshale discussed in Li and Einstein (2019). The loading conditions are shown schematically in Figure 1.

The uniaxial compression tests were conducted on intact 101.6 mm × 50.8 mm × 25.4 mm specimens under load control at a rate of 82.56 N/s (see Figure 2a for loading curve) in the 200,000 lb capacity Baldwin load frame (see Morgan et al., 2013, for details on the loading machine), and the final crack patterns are shown in Figure 3. In the Opalinus specimen, the bedding planes were oriented vertically, that is, in-plane with the loading direction.

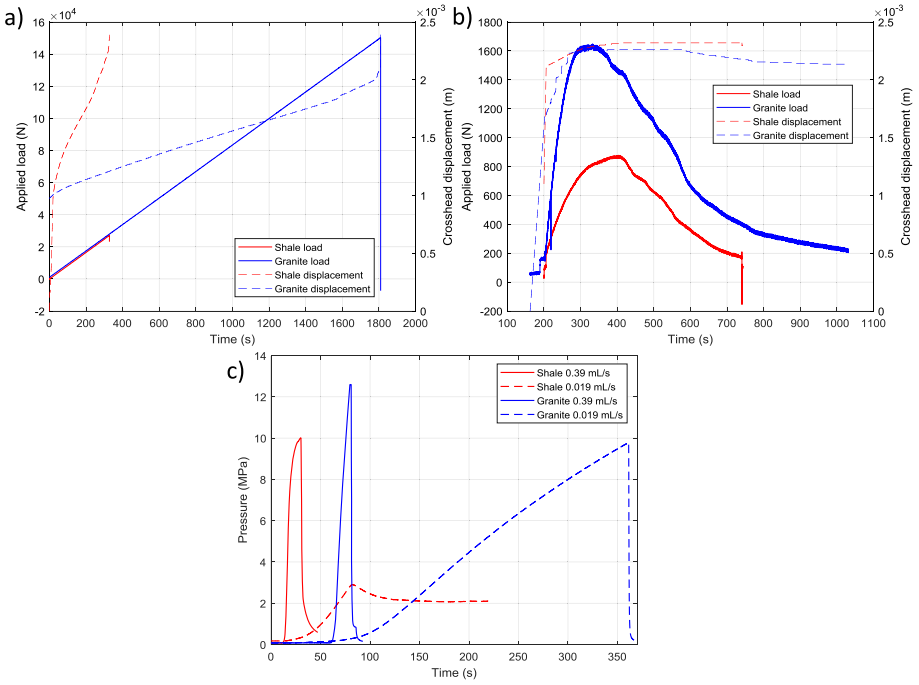

Figure 2. (a) Load-displacement data over time for granite intact uniaxial compression test and Opalinus intact uniaxial compression test. (b) Load-displacement data over time for granite and shale beam bending tests. (c) Pressure over time from hydraulic fracturing experiments.

The beam bending experiments were conduced on 241.3 mm × 50.8 mm × 25.4 mm specimens with a 1 cm precut notch supported on roller and pin connections on the bottom and cylindrical loading platens on the top. The specimen was loaded on crack mouth opening control at a rate of 0.0127 mm/min (see Figure 2b for loading curve). In the Opalinus specimen, the bedding planes were oriented horizontally.

The HF experiments were conducted on 152.4 mm × 76.2 mm × 25.4 inch specimens with a single 12.7 mm precut notch in the granite and 101.6 mm × 50.8 mm × 25.4 mm specimens with a single 8.47 mm precut notch in the shale. Note that different specimen sizes are used as different pressurization enclosures are required to generate hydraulic fractures in each material. All HF experiments are conducted under a uniaxial load of 3.5 MPa, using nominal flow rates of 0.39 and 0.019 ml/s (see Figure 2c for loading curve). In the Opalinus specimen, the bedding planes are oriented vertically.

2.2.2. Calculation of External Mechanical Work

To calculate the work done by the loading machine during beam bending or uniaxial compression tests, we consider the load-displacement curves shown in Figure 4, and numerically integrate as $W = \int Fds$, where W is work done, F is the force applied, and s is the crosshead displacement. The integration is calculated between the green and red dotted lines for shale and between the green and blue dotted lines for granite.

For the HF experiments, we similarly numerically integrate the pressure-volume curve as $W = \int PdV$. However, in our setup the deformation of the pump and piping contribute significantly to the pressure-volume response. To quantify and account for this effect, we conducted a system compliance test where a stopper was inserted before the HF enclosure to isolate the pressure-volume response of the tubing and pump as shown in Figure 5a. The data are shown in the red curve in Figure 5b and compared to the blue curve, which is the pressure-volume response without the stopper, that is, with the enclosure and a granite specimen. We see that the HF device with a granite specimen has a system compliance of 2.833 MPa/cm^3; that is 1 cm^3 of injected fluid increases fluid pressure by 2.83 MPa. With the stopper, the system compliance increases to 7.25 MPa/cm^3; that is 1 cm^3 increases pressure by 7.25 MPa. The difference between these compliances then is the compliance of the HF enclosure and granite specimen, for which 1 cm^3 of fluid injection increases the pressure by 7.25–2.83 = 4.42 MPa. Using this calibration and assuming a linear pressure-volume curve, we can then estimate work done by the fluid as

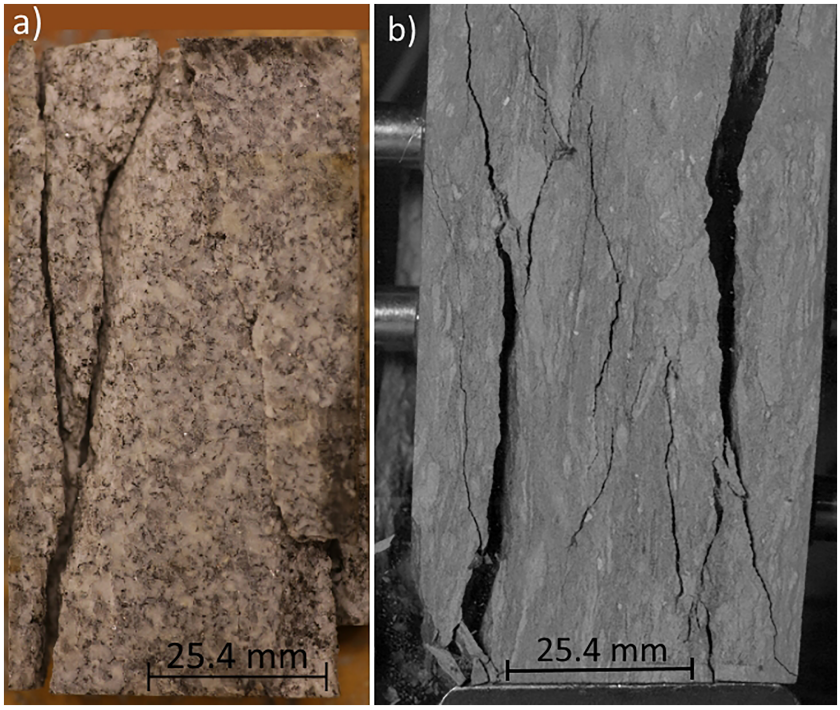

Figure 3. Final crack pattern of (a) granite intact uniaxial compression test and (b) Opalinus intact uniaxial compression test.

$$\tilde{E}_{fluid} = \frac{1}{4.42 \times 10^{12} \quad Pa/m^3} \frac{1}{2} P_{max}^2. \tag{1}$$

2.2.3. Acoustic Emissions Setup

Each test was instrumented with eight Micro30S sensors from Physical Acoustic Corporation, sampled at 5 MHz using four PCI-2 data acquisition cards. The sensors were coupled with 3 M 0.002″ acrylic tape to the specimen, and sensors in the load path were emplaced within an inset in the loading platens. We observe generally similar noise levels in all experiments. Sensor locations are shown in Figure 1. A total of 20 and 60 dB of preamplification were used in the granite and shale tests, respectively. The sensors exhibit a frequency range of 125 to 400 kHz, with a resonant frequency of 225 kHz. Locations are calculated in granite using a *P* wave velocity of 4,500 m/s and error tolerance of 5 mm, and in Opalinus clayshale using an elliptical velocity distribution, with a *P* wave velocity of 3,500 m/s along the bedding plane, and 2,000 m/s across

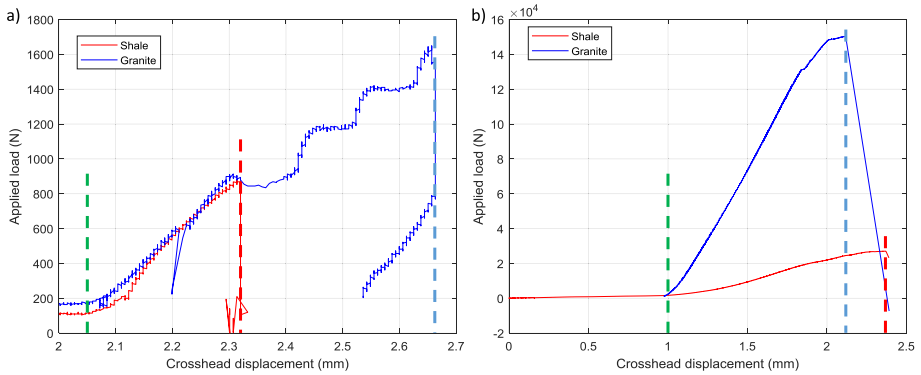

Figure 4. (a) Load-displacement data from beam bending experiments. (b) Load-displacement data from uniaxial compression experiments. Green dotted lines indicate left bounds of numerical integration, and red and blue dotted lines indicate right bounds of numerical integration for shale and granite, respectively.

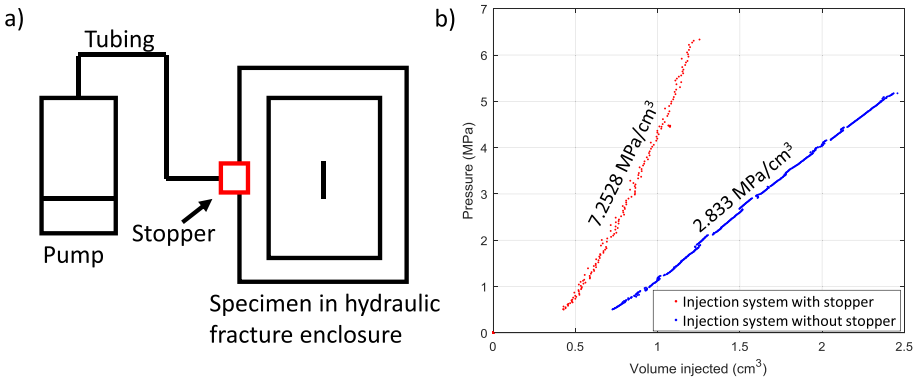

Figure 5. (a) Schematic of setup used to determine pressure-volume response of tubing and pump versus the response of the fluid in the enclosure. (b) Pressure-volume data for HF setup with and without the stopper.

bedding planes, to an error tolerance of 10 mm. In our algorithm, the location error is defined, per channel, as the *P* wave velocity multiplied by the difference between the observed arrival time and the predicted travel time between the inverted source location and the sensor. The location error must be less than the error tolerance on all detected channels and be detected by a minimum of four channels to be considered an event. The *P* wave velocities were measured under experimental conditions. More details of the AE setup can be found in Li et al. (2019). First motion polarities are picked on the peak succeeding the first arrival, and moment tensor inversion calculation using the SiGMA method proposed by Ohtsu (2000). Moment tensors are then decomposed into double couple (DC), compensated linear vector dipole, and isotropic (ISO) components using the formulation proposed by Vavrycuk (2011).

The radiated seismic energy is estimated from each experiment by first calibrating all AE amplitudes to moment magnitudes (M_0) using a ball drop as described in McLaskey et al. (2015). The specific methodology is documented for the beam bending test in Li and Einstein (2017) and is applied to all other tests presented in this study. We briefly outline the methodology here. In each test we attach the sensors and connect all the acquisition equipment; we then drop a 1.58 mm steel ball from a height of 10 cm and record the waveforms resulting from the ball impact and subsequent bounces. The ball drop is repeated 10 times, and then the fracturing experiment is conducted. We then compare events with different amplitudes from the experiment to the ball drop waveforms and compare them in the frequency domain to calculate M_w for each of the three events. We then fit a calibration curve between the first arrival amplitude of each AE event to its M_w and apply this calibration curve to the entire catalog of first arrival amplitudes to calculate M_w for the entire catalog. *b* values and their standard deviations are then estimated based on the maximum likelihood method developed by Bender (1983) using a bin size of 0.1, and the magnitude of completeness is estimated from the resulting cumulative magnitude-frequency plot. While this magnitude calibration method implicitly accounts for nonlinearity in the sensors and the difference in attenuation between granite and shale since it empirically incorporates the Green's function between the source and the recorded signal, we nevertheless estimate the attenuation factor of the two materials for clarity. We estimate the *P* wave attenuation coefficient Q_P of granite to be 8.41 in the 100–200 kHz range, and similarly 16.81 in the shale (see Supporting Information S1 for details). These attenuation coefficients, when applied to a *P* wave propagating across the specimen, reduce the amplitude by 37% in shale and 16% in granite, which cannot account for the differences seen in section 3.

We then estimate total radiated seismic energy (E_R) by calculating the M_0 of each event detected during the test, summing these M_0 to calculate the total transformed M_0, and estimating radiated seismic energy assuming a constant ratio $\frac{E_R}{M_0}$ for all events. The question of the value of this ratio is discussed in Goodfellow et al. (2015), and we present a summary here. Based on fracture mechanics, Kanamori (1978) suggests that the radiated seismic energy can be estimated as $M_0(\Delta\sigma/2\mu)$, where $\Delta\sigma$ is the stress drop during an earthquake and μ is the shear modulus. The stress drop can then be related to the apparent stress on the fault as $\sigma_a \sim \Delta\sigma/2$. For large earthquakes, they estimate (Kanamori & Anderson, 1975; Wyss & Brune, 1968) that the apparent stress is approximately 1 MPa, resulting in $\frac{E_R}{M_0} = 5 \times 10^{-5}$. For microearthquakes and nanoearthquakes observed during field and laboratory tests, Goodfellow and Young (2014) suggest that apparent stress is between 0.01 and 0.1 MPa. We make the assumption in our study that the apparent stress

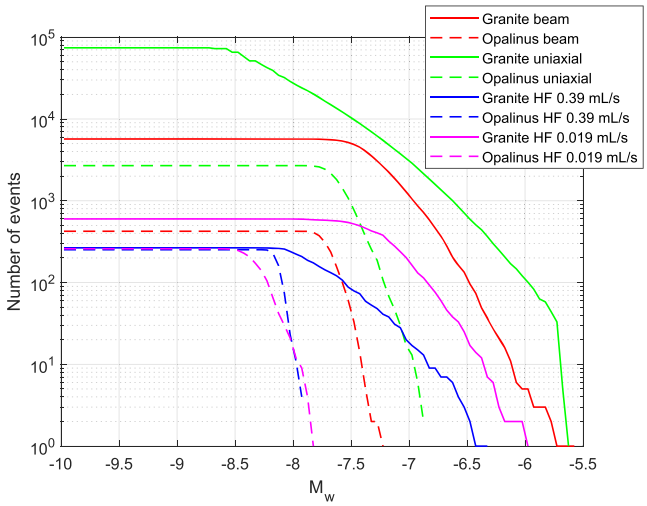

Figure 6. Cumulative magnitude-frequency plots for all experiments.

is 0.1 MPa, hence $\frac{E_R}{M_0} = 5 \times 10^{-6}$, which lies on the lower end of the 0.1 to 10 MPa apparent stress range as calculated by Ide and Beroza (2001) for earthquakes between $M_w = -3.5$ and $M_w = 8$. Note that for HF tests, only the injection stage is considered, and not the initial loading stage, as the in situ stress is held constant throughout each experiment, and we are most interested in the creation of fractures and microfractures as a result of elevated fluid pressure.

2.2.4. Estimation of Microcrack Zone Velocity

For the beam bending and HF experiments, we additionally estimate the propagation velocity of the microcracked zone based on imaging data (Li & Einstein, 2019) captured by a high magnification lens and analyzed using digital image correlation technologies. The velocity is estimated at the location of the furthest extent of high strain on consecutive images in time.

3. Results

Based on the methodology described in section 2.2.3, we calculate the magnitudes for all events in each experiment and present them as cumulative magnitude frequency plots shown in Figure 6. *b* values and magnitudes of completion for each experiment are presented in Table 1 alongside the cumulative radiated seismic energy E_R and external work $\tilde{E}$.

In general, the radiated seismic energy of Opalinus clayshale is 2 to 3 orders of magnitude smaller than the granite. Also, the uniaxial compression tests radiate significantly more seismic energy than the other loading mechanisms. If we consider this information from the perspective of the cumulative magnitude frequency

Table 1
Summary of Magnitude of Completeness (M_c), Number of Events N, and b Values, Based on Figure 6

Material	Loading condition	M_c	N	b	E_R (J)	$\tilde{E}$ (J)
Barre granite	Four-point beam bending	−7.30	5694	1.62 ± 0.03	9.84×10^{-4}	6.97×10^{-1}
Opalinus BMA-2	Four-point beam bending	−7.70	424	4.09 ± 0.27	8.94×10^{-6}	2.19×10^{-1}
Barre granite	Intact uniaxial compression	−8.50	74226	0.82 ± 0.003	4.33×10^{-3}	1.12×10^{2}
Opalinus BMA-2	Intact uniaxial compression	−7.65	2691	2.35 ± 0.05	9.04×10^{-5}	2.07×10^{1}
Barre granite	HF Q = 0.39 ml/s	−8.05	266	0.79 ± 0.05	1.80×10^{-5}	1.77×10^{1}
Opalinus BMA-2	HF Q = 0.39 ml/s	−8.10	252	7.58 ± 0.88	1.05×10^{-6}	4.77×10^{0}
Barre granite	HF Q = 0.019 ml/s	−7.20	600	1.51 ± 0.08	1.40×10^{-4}	1.02×10^{1}
Opalinus BMA-2	HF Q = 0.019 ml/s	−8.30	259	3.18 ± 0.27	7.18×10^{-7}	1.02×10^{0}

Note. Radiated seismic energy (E_R) and external work done ($\tilde{E}$) are also shown for each experiment, as calculated by methods described in sections 2.2.3 and 2.2.2, respectively.

Table 2
Table Summarizing Seismic Kinetics and Kinematics of Various Tests

Material	Loading condition	$E_R/\tilde{E}$	DC (%)	+ISO (%)	−ISO (%)	$\frac{(E_R/\tilde{E})_{Opalinus}}{(E_R/\tilde{E})_{Granite}}$ (%)	Microcracked zone velocity (mm/s)
Barre granite	Four-point beam bending	1.41×10^{-3}	52.7	32.7	−3.6		0.057
Opalinus BMA-2	Four-point beam bending	4.07×10^{-5}	42.1	34.3	−10.4	2.9	0.077
Barre granite	Intact uniaxial compression	3.87×10^{-5}	50.1	25.4	−13.1		
Opalinus BMA-2	Intact uniaxial compression	4.37×10^{-6}	46.8	15.3	−25.7	11.3	
Barre granite	HF Q = 0.39 ml/s	1.02×10^{-6}	52.1	27.7	−9.3		1.07
Opalinus BMA-2	HF Q = 0.39 ml/s	2.21×10^{-7}	52.9	15.8	−20.2	21.7	1.43
Barre granite	HF Q = 0.019 ml/s	1.37×10^{-5}	46.8	32.0	−8.8		0.022
Opalinus BMA-2	HF Q = 0.019 ml/s	7.06×10^{-7}	36.9	17.4	−32.2	5.2	0.377

Note. $E_R/\tilde{E}$ is calculated from data presented in Table 1, and the focal mechanism proportions are shown for each test. DC denotes the mean proportion of the moment tensor, which can be explained by a double-couple mechanism; +ISO and −ISO denote the mean proportion of expansive and implosive isotropic components of moment tensor. The $\frac{(E_R/\tilde{E})_{Opalinus}}{(E_R/\tilde{E})_{Granite}}$ column shows the ratio of Opalinus to Granite normalized radiated seismic energy for each loading case. The last column lists estimated propagation velocity of the microcracked zone, estimated as described in section 2.

plots shown in Figure 6, then we see that the difference between Opalinus and Granite can be explained through two factors. First, many more events are detected in Granite than Opalinus, particularly in the dry (uniaxial and beam bending) experiments. Second, the slope of the cumulative magnitude frequency plots, that is, the *b* value, is around 0.8 to 1.6 for the granite, which agrees with some previous experimental studies (Amitrano, 2003; Scholz, 1968), and significantly larger for the Opalinus, even considering the errors in the *b* values estimates. This difference in *b* value suggests that Opalinus produces more smaller events and fewer larger AE events when compared to the granite, which is in agreement with field data from Gale et al. (2014), who note that clay-rich shale rocks exhibit fewer large fractures than other rocks.

Regarding the external work done by the loading machine or injection fluid, the methods described in section 2.2.2 were applied to each experiment, and the results are shown in Table 1. The fluid injection energies are similar to those reported in Goodfellow et al. (2015) (they calculate between 7.5 and 26.5 J under triaxially confined conditions), and we can see that the work done during the beam bending tests is an order of magnitude smaller than the HF tests, which are an order of magnitude smaller than in the uniaxial compression tests.

Given the radiated seismic energy estimates and the work values shown in Table 1, we can estimate the normalized radiated seismic energy $E_R/\tilde{E}$ as shown in Table 2. These are presented alongside the relative proportion of DC and ISO components as calculated from moment tensor decomposition from each experiment. We also calculate the ratio of normalized seismic energy between Granite and Opalinus and compare them to estimates of the propagation velocity of the microcracked zone. These will be discussed in the following section.

4. Discussion

4.1. Difference Between Barre Granite and Opalinus Clayshale

Firstly, we can see that the ratio $\frac{(E_R/\tilde{E})_{Opalinus}}{(E_R/\tilde{E})_{Granite}}$ shown in Table 2 varies between 3% to 22% across the four loading mechanisms, which indicates that the Opalinus clayshale consistently radiates less seismic energy per unit work done than the granite. Specifically, the ratio varies by less than an order of magnitude across multiple loading mechanisms, suggesting that this ratio is to some extent a material property. We suggest that this is due to differences in the micromechanical friction properties between the two rocks. This was also noted by Kohli and Zoback (2013), who found that shales tended to become increasingly aseismic with increased clay and organic content. Similarly, the shale in our study contains higher clay content and is thus generally more ductile than the granite, which suggests that slip events in the granite may be more likely to rupture rapidly compared to the shale. This is reflected in the focal mechanisms; for example, we can see in Table 2 that the proportion of DC (shear) focal mechanisms is generally higher in granite than in the shale. In contrast, the proportion of volume reduction (−ISO) focal mechanisms in shale is higher than granite, suggesting that closure of pore space or bedding planes are significant factors in shale behavior even in tensile stress regimes as generated by HF or beam bending.

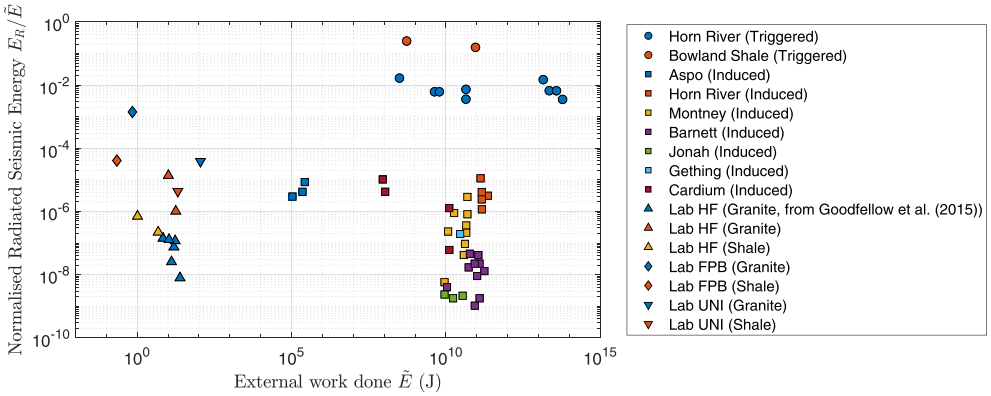

Figure 7. Comparison of normalized radiated seismic energy with other laboratory and field studies. Aspo data collected from study by Kwiatek et al. (2018); field and other lab data collected from study by Goodfellow et al. (2015). HF = hydraulic fracturing; FPB = four-point bending; UNI = uniaxial compression.

4.2. Effect of Loading Condition

Regarding the effect of the loading condition, we can see (Table 2) that the beam bending is the most efficient (highest $E_R/\tilde{E}$), followed by the uniaxial compression tests, then the slow HF tests, and that the high injection rate HF tests are least efficient. The observation that the hydraulic fracture tests radiate the least seismic energy per unit work done can be related to Cappa et al. (2019), who found in a laboratory study that faults became increasingly aseismic with increasing fluid pressure.

Among the HF tests, we observe elevated $E_R/\tilde{E}$ in the lower injection rate tests compared to the high injection rate tests. Among the dry tests, we see higher $E_R/\tilde{E}$ in the beam bending compared to the uniaxial compression tests. This suggests there is some relationship between loading rate and the seismic energy emitted; however, we find that the literature on this topic is inconclusive. For example, Mair et al. (2007), who conducted direct shear tests on artificial fault gouge, found increased seismicity per unit distance of slip at lower slip rates, while Backers et al. (2005), who conducted beam bending tests on sandstone at a variety of loading rates, found seismic energy was positively related to loading rate. This disparity, as well as our results, suggests that the radiated energy is a complex phenomenon that is dependent on many parameters beyond loading rate and material and merits further study.

The microcrack zone velocity is presented alongside the normalized radiated seismic energy in Table 2. We can see that, generally, normalized radiated seismic energy is inversely related to the microcrack propagation velocity. Similarly, the larger velocity difference between the two granite HF tests compared to the Opalinus HF tests is reflected in the normalized radiated seismic energy, which also varies by a larger factor between the granite HF tests than the Opalinus HF tests.

4.3. Comparison to Other Studies

We compare our measurements of normalized radiated seismic energy to previous laboratory and field studies, as shown in Figure 7. We can see that, in general, our HF results on granite are consistent with induced seismicity in the field and with estimates from the underground laboratory in Aspo. We find that in general, our estimates are slightly higher than those measured by Goodfellow et al. (2015), which may be due to the compliance of the pumping equipment that was accounted for in our study, but not in theirs.

5. Conclusions

Recall that the goal of this study was to gain an understanding of how the radiated seismic energy normalized by external work done is related to different loading mechanisms and to different materials, namely, Opalinus clayshale and Barre granite. Specifically, we calculate the external work done on the rock and estimate the radiated seismic energy from four-point beam bending, intact uniaxial compression, and HF experiments. We find that the radiated seismic energy, when normalized by the external work, varies significantly across loading mechanisms. We find that HF experiments emit significantly less-normalized radiated seismic energy than the dry tests and that among the HF tests, the higher injection rate tests tended to be more aseismic. Similarly in the dry tests, we find that the uniaxial compression test is more aseismic than

the beam bending test, and as a result suggest that loading rate is inversely proportional to the normalized radiated seismic energy. We also find that the normalized radiated seismic energy is inversely related to the growth rate of the microcracked zone.

On the difference between shale and granite, we find that the normalized radiated seismic energy in shale to be 3% to 22% of that in granite across the multiple loading mechanisms. We suggest that this can be attributed to the higher clay content in the shale, which has been previously shown to be related to aseismicity. Although all these observations are made at the laboratory scale, there are numerous analogous field observations. Given the importance of induced seismicity, better understanding of the phenomena leading to radiation of seismic energy, as discussed in this paper, is necessary.

Acknowledgments
The authors would like to thank Douglas Schmitt, Georg Dresen, and an anonymous reviewer for their excellent comments and suggestions on the manuscript. The authors would also like to thank Total SA and the Abu Dhabi National Oil Company for funding this research and the Mont Terri Rock Laboratory for their generous donation of Opalinus clayshale. Finally, we would like to thank Wei Li and Omar Aldajani for their assistance with experiments and Professors John Germaine, Brian Evans, and German Prieto for invaluable advice. The processed data set can be found online at (https://doi.org/10.17632/gjtv7w5wbk).

References

Amitrano, D. (2003). Brittle ductile transition and associated seismicity: Experimental and numerical studies and relationship with the b value. *Journal of Geophysical Research*, *108*(B1), 2044. https://doi.org/10.1029/2001JB000680

Backers, T., Stanchits, S., & Dresen, G. (2005). Tensile fracture propagation and acoustic emission activity in sandstone: The effect of loading rate. *International Journal of Rock Mechanics and Mining Sciences*, *42*, 1094–1101.

Bender, B. (1983). Maximum likelihood estimation of b values for magnitude grouped data. *Bulletin of the Seismological Society of America*, *73*(3), 831–851.

Cappa, F., Scuderi, M. M., Collettini, C., Guglielmi, Y., & Avouac, J.-P. (2019). Stabilization of fault slip by fluid injection in the laboratory and in situ. *Science Advances*, *5*(3), eaau4065.

Ellsworth, W. L. (2013). Injection-induced earthquakes. *Science*, *341*(6142), 1225942.

Gale, J. F., Laubach, S. E., Olsen, J. E., Eichhubl, P., & Fall, A. (2014). Natural fractures in shale: A review and new observations. *AAPG Bulletin*, *98*(11), 2165–2216.

Goldsmith, W., Sackman, J. L., & Ewerts, C. (1976). Static and dynamic fracture strength of barre granite. *International Journal of Rock Mechanics and Mining Sciences and Geomechanics Abstracts*, *13*(11), 303–309.

Goodfellow, S., Nasseri, M., Maxwell, S., & Young, R. (2015). Hydraulic fracture energy budget: Insights from the laboratory. *Geophysical Research Letters*, *42*, 3179–3187. https://doi.org/10.1002/2015GL063093

Goodfellow, S., & Young, R. (2014). A laboratory acoustic emission experiment under in situ conditions. *Geophysical Research Letters*, *41*, 3422–3430. https://doi.org/10.1002/2014GL059965

Grigoli, F., Cesca, S., Rinaldi, A. P., Manconi, A., Lopez-Comino, J. A., Clinton, J. F., et al. (2018). The november 2017 mw 5.5 Pohang earthquake: A possible case of induced seismicity in South Korea. *Science*, *360*(6392), 1003–1006.

Ide, S., & Beroza, G. C. (2001). Does apparent stress vary with earthquake size? *Geophysical Research Letters*, *28*(17), 3349–3352.

Jestin, C., Lengline, O., & Schmittbuhl, J. (2019). Energy partitioning during subcritical mode i crack propagation through a heterogeneous interface. *Journal of Geophysical Research: Solid Earth*, *124*, 837–855. https://doi.org/10.1029/2018JB016831

Kanamori, H. (1978). Quantification of earthquakes. *Nature*, *271*, 411–414.

Kanamori, H., & Anderson, D. L. (1975). Theoretical basis of some empirical relations in seismology. *Bulletin of the Seismological Society of America*, *65*(5), 1073–1095.

Kohli, A. H., & Zoback, M. D. (2013). Frictional properties of shale reservoir rocks. *Journal of Geophysical Research: Solid Earth*, *118*, 5109–5125. https://doi.org/10.1002/jgrb.50346

Kwiatek, G., Martnez-Garzon, P., Plenkers, K., Leonhardt, M., Zang, A., von Specht, S., et al. (2018). Insights into complex subdecimeter fracturing processes occurring during a water injection experiment at depth in Aspo Hard Rock Laboratory, Sweden. *Journal of Geophysical Research: Solid Earth*, *123*, 6616–6635. https://doi.org/10.1029/2017JB014715

Li, B. Q. (2019). *Microseismic and real-time imaging of fractures and microfractures in Barre granite and Opalinus clayshale* (Doctoral Dissertation). Cambridge, MA: Massachusetts Institute of Technology. Accessed at DSpace http://dspace.mit.edu/handle/1721.1/7582

Li, B. Q., & Einstein, H. H. (2017). Comparison of visual and acoustic emission observations in a four point bending experiment on barre granite. *Rock Mechanics and Rock Engineering*, *1*, 2277–2296.

Li, B. Q., & Einstein, H. H. (2019). Direct and microseismic observations of hydraulic fracturing in Barre granite and Opalinus clayshale. *Journal of Geophysical Research: Solid Earth*, *124*, 11,900–11,916. https://doi.org/10.1029/2019JB018376

Li, B. Q., Gonçalves da Silva, B. M., & Einstein, H. H. (2019). Laboratory hydraulic fracturing of granite: Acoustic emission observations and interpretation. *Engineering Fracture Mechanics*, *209*, 200–220.

Mair, K., Marone, C., & Young, R. P. (2007). Rate dependence of acoustic emissions generated during shear of simulated fault gouge. *Bulletin of the Seismological Society of America*, *97*(6), 1841–1849.

Mazzoldi, A., Rinaldi, A. P., Borgia, A., & Rutqvist, J. (2012). Induced seismicity within geological carbon sequestration projects: Maximum earthquake magnitude and leakage potential from undetected faults. *International Journal of Greenhouse Gas Control*, *10*, 434–442.

McLaskey, G. C., Lockner, D. A., Kilgore, B. D., & Beeler, N. M. (2015). A robust calibration technique for acoustic emission systems based on momentum transfer from a ball drop. *Bulletin of the Seismological Society of America*, *105*, 257–271.

Morgan, S. P., Johnson, C. A., & Einstein, H. H. (2013). Cracking processes in barre granite: fracture process zones and crack coalescence. *International Journal of Fracture*, *180*, 177–204.

Murthy, V. R. (1957). *Bed rock geology of the east barre area, Vermont* (Tech. Rep.). Vermont Geological Survey

Ohtsu, M. (2000). Moment tensor analysis of AE and sigma code. *Acoustic emission-beyond the millennium* (pp. 19–34). Berlin: Springer.

Scholz, C. H. (1968). The frequency-magnitude relation of microfracturing in rock and its relation to earthquakes. *Bulletin of the Seismological Society of America*, *58*(1), 399–415.

Teran, O., & Thornton, M. (2019). Microseismic bedding-plane slip theory—[Requires] a very slippery slope or a very large SHmax. In *Unconventional resources technology conference*. Denver, CO. https://doi.org/10.15530/urtec-2019-997

Thomas, M. Y., Lapusta, N., Noda, H., & Avouac, J.-P. (2014). Quasi-dynamic versus fully dynamic simulations of earthquakes and aseismic slip with and without enhanced coseismic weakening. *Journal of Geophysical Research: Solid Earth*, *119*, 1986–2004. https://doi.org/10.1002/2013JB010615

Vavrycuk, V. (2011). Tensile earthquakes: theory, modelling, and inversion. *Journal of Geophysical Research*, *116*, B12320. https://doi.org/10.1029/2011JB008770

Wyss, M., & Brune, J. N. (1968). Seismic moment, stress and source dimensions for earthquakes in the California-Nevada region. *Journal of Geophysical Research*, *73*, 4681–4694.

Yoshimitsu, N., Kawakata, H., & Takahashi, N. (2014). Magnitude -7 level earthquakes: A new lower limit of self-similarity in seismic scaling relationships. *Geophysical Research Letters*, *41*, 4495–4502. https://doi.org/10.1002/2014GL060306